

Moving gravitational lenses: imprints on the CMB

N. Aghanim¹, S. Prunet¹, O. Forni¹, and F. R. Bouchet²

¹ IAS-CNRS, Université Paris XI, Bâtiment 121, F-91405 Orsay Cedex

² IAP-CNRS, 98 bis, Boulevard Arago, F-75014 Paris

Received date / accepted date

Abstract. With the new generation of instruments for Cosmic Microwave Background (CMB) observations aiming at an accuracy level of a few percent in the measurement of the angular power spectrum of the anisotropies, the study of the contributions due to secondary effects has gained impetus. Furthermore, a reinvestigation of the main secondary effects is crucial in order to predict and quantify their effects on the CMB and the errors that they induce in the measurements.

In this paper, we investigate the contribution, to the CMB, of secondary anisotropies induced by the transverse motions of clusters of galaxies. This effect is similar to the Kaiser–Stebbins effect. In order to address this problem, we model the gravitational potential well of an individual structure using the Navarro, Frenk & White profile. We generalise the effect of one structure to a population of objects predicted using the Press-Schechter formalism. We simulate maps of these secondary fluctuations, compute the angular power spectrum and derive the average contributions for three cosmological models. We then investigate a simple method to separate this new contribution from the primary anisotropies and from the main secondary effect, the Sunyaev-Zel’dovich kinetic effect from the lensing clusters.

Key words: Cosmology: cosmic microwave background – gravitational lensing – secondary fluctuations – clusters of galaxies

1. Introduction

During the next decade, several experiments are planned to observe the Cosmic Microwave Background (CMB) and measure its temperature fluctuations (Planck surveyor, Map, Boomerang, ...). Their challenge is to measure the small scales anisotropies of the CMB (a few arcminutes up to ten degrees scale) with sensitivities better by a factor 10 than the COBE satellite (Smoot et al. 1992). These high sensitivity and resolution measurements will

tightly constrain the value of the main cosmological parameters (Kamionkowski et al. 1994). However, the constraints can only be set if we are able to effectively measure the *primary* temperature fluctuations. These fluctuations, present at recombination, give an insight into the early universe since they are directly related to the initial density perturbations which are the progenitors to the cosmic structures (galaxies and galaxies clusters) in the present universe; but which are first and foremost the relics of the very early initial conditions of the universe.

Between recombination and the present time, the CMB photons could have undergone various interactions with the matter and structures present along their lines of sight. Some of these interactions can induce additional temperature fluctuations called, *secondary* anisotropies because they are generated after the recombination. Along a line of sight, one measures temperature fluctuations which are the superposition of the *primary* and *secondary* anisotropies. As a result, and in the context of the future CMB experiments, accurate analysis of the data will be needed in order to account for the foreground contributions due to the secondary fluctuations. Photon–matter interactions between recombination and the present time are due to the presence of ionised matter or to variations of the gravitational potential wells along the lines of sight.

The CMB photons interact with the ionised matter mainly through Compton interactions. In fact, after recombination the universe could have been re-ionised globally or locally. Global early re-ionisation has been widely studied (see Dodelson & Jubas 1995 for a recent review and references therein). Its main effect is to either smooth or wipe out some of the primary anisotropies; but the interactions of the photons with the matter in a fully ionised universe can also give rise to secondary anisotropies through the Vishniac effect (Vishniac 1987). This second order effect has maximum amplitudes for a very early re-ionisation. The case of a late inhomogeneous re-ionisation and its imprints on the CMB fluctuations has been investigated (Aghanim et al. 1996) and found to be rather important. In this case, the secondary anisotropies are due to the bulk motion of ionised clouds with respect to the CMB frame. When the re-ionisation

is localised in hot ionised intra-cluster media the photons interact with the free electrons. The inverse Compton scattering between photons and electrons leads to the so-called Sunyaev-Zel'dovich (hereafter SZ) effect (Sunyaev & Zel'dovich 1972, 1980). The Compton distortion due to the motion of the electrons in the gas is called the thermal SZ effect. The kinetic SZ effect is a Doppler distortion due to the peculiar bulk motion of the cluster with respect to the Hubble flow. The SZ thermal effect has the unique property of depressing the CMB brightness in the Rayleigh-Jeans region and increasing its brightness above a frequency of about 219 GHz. This frequency dependence makes it rather easy to observe and separate from the kinetic SZ effect. In fact, the latter has a black body spectrum which makes the spectral confusion between kinetic SZ and primary fluctuations a serious problem. The SZ effect has been widely studied for individual clusters and for populations of clusters. For full reviews on the subject we refer the reader to two major articles: Rephaeli 1995 and Birkinshaw 1997. These investigations have clearly shown that the SZ effect in clusters of galaxies provides a powerful tool for cosmology through measurements of the Hubble constant, the radial peculiar velocity of clusters and consequently the large scale velocity fields.

Besides the interactions with the ionised matter, some secondary effects arise when the CMB photons traverse a varying gravitational potential well. In fact, if the gravitational potential well crossed by the photons evolves between the time they enter the well and the time they leave it, the delay between entrance and exit is equivalent to a shift in frequency, which induces a temperature anisotropy on the CMB. This effect was first studied by Rees & Sciama (1968) for a potential well growing under its own gravity. Numerous authors have investigated the potential variations due to collapsing objects and their effect on the CMB (Kaiser 1982, Nottale 1984, Martínez-González, Sanz & Silk 1990, Seljak 1996). Similarly, a gravitational potential well moving across the line of sight is equivalent to a varying potential and will thus imprint secondary fluctuations on the CMB. This effect was first studied for one cluster of galaxies by Birkinshaw & Gull (1983) (Sect. 2). Kaiser & Stebbins (1984) and Bouchet, Bennett & Stebbins (1988) investigated a similar effect for moving cosmic strings. Recent work (Tuluie & Laguna 1995, Tuluie, Laguna & Anninos 1996) based on N-body simulations has pointed out this effect in a study of the effect of varying potential on rather large angular scales ($\simeq 1^\circ$). A discussion of some of these results and a comparison with ours will follow in the next sections.

In this paper, following the formalism of Birkinshaw & Gull (1983) and Birkinshaw (1989), we investigate the contribution of secondary anisotropies due to a population of collapsed objects moving across the line of sight, these objects range from small groups to rich clusters in scale (10^{13} to $10^{15} M_\odot$). In section 2., we first study in detail the case of a unique collapsed structure. We use a

structure model to compute in particular the deflection angle and derive the spatial signature of the moving lens effect. We then account (Section 3.) for the contribution, to the primordial cosmological signal, of the whole population of collapsed objects using predicted counts and we simulate maps of these secondary anisotropies. In section 4., we analyse the simulated maps and present our results. We give our conclusions in section 5.

2. Formalism for an individual moving structure

One of the first studies of the photon-gravitational potential well interactions is related to the Sachs-Wolfe effect (Sachs & Wolfe 1967). At the recombination time ($z \simeq 1100$) the photons and matter decouple while they are in potential wells; the photons are redshifted when they leave the potential wells. This generates the large angular scale temperature fluctuations.

Other authors have investigated the effect of time varying potentials on the CMB photons after the recombination, namely the Rees-Sciama effect (Rees & Sciama 1968). If the potential well crossed by the photons evolves between the time they enter and their exit, the extra-time delay they suffer changes the temperature of the CMB and induces an additional anisotropy. The variation of the potential well can have an ‘‘intrinsic’’ or a ‘‘kinetic’’ origin. The first case describes the evolution with respect to the background density distribution. The second case is related to the bulk motion of a gravitational potential well across the line of sight which mimics a time variation of the potential. Photons crossing the leading edge of a structure will be redshifted because of the increasing depth of the potential well during their crossing time; while photons crossing the trailing edge of the same structure are blueshifted. This results in a characteristic spatial signature for the induced anisotropy: a hot-cold temperature spot.

The specific effect of a moving cluster across the sky was first studied by Birkinshaw & Gull (1983) (correction to this paper was made in Birkinshaw 1989) and it was invoked as a method to measure the transverse velocity of massive clusters of galaxies. These authors found that the transverse motion of a cluster across the line of sight induces a frequency shift given by:

$$\frac{\Delta\nu}{\nu} = \beta\gamma \sin\alpha \cos\phi \delta(\mathbf{b}). \quad (1)$$

Here, β is the peculiar velocity in units of the speed of light ($\beta = v/c$), γ is the Lorentz factor ($\gamma = (1 - \beta^2)^{-1/2}$), α and ϕ are respectively the angle between the peculiar velocity \mathbf{v} and the line of sight of the observer and the azimuthal angle in the plane of the sky, and $\delta(\mathbf{b})$ is the deflection angle due to the gravitational lensing by the cluster at a distance equal to the impact parameter \mathbf{b} . This frequency shift induces a brightness variation which in turn can be expressed as a secondary temperature fluctuation $\delta T/T$.

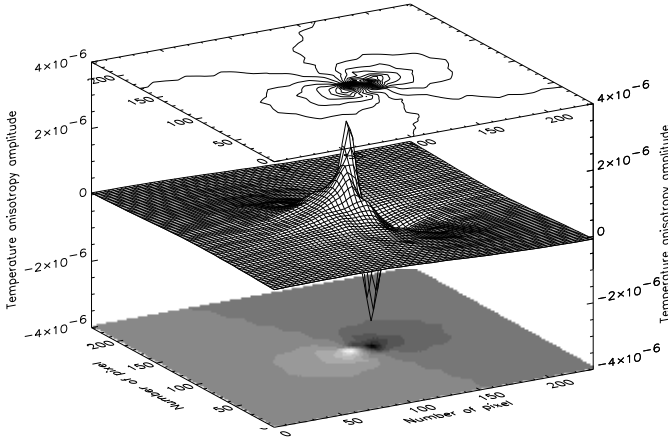


Fig. 1. Characteristic spatial signature of a temperature fluctuation due to a moving lens with mass $M = 10^{15} M_{\odot}$ and velocity $v = 600$ km/s.

In their paper, Birkinshaw & Gull derived an expression for $\delta T/T$ in the Rayleigh-Jeans regime, with some specific assumptions on the gravitational potential well associated with the cluster. They assumed that the matter in the galaxy cluster was homogeneously distributed in an isothermal sphere of radius R , where R is the characteristic scale of the cluster.

In our paper, we basically follow the same formalism as Birkinshaw & Gull’s using the corrected expression from Birkinshaw 1989. We compute the gravitational deflection angle at the impact parameter $\delta(\mathbf{b})$, the corresponding frequency shift and then derive the associated temperature fluctuation. The main difference between our approach in this section and the previous work concerns the physical hypothesis that we adopt to describe the distribution of matter in the structures. In fact, in order to derive the deflection angle, we find the homogeneous isothermal distribution a too simple and rather unrealistic hypothesis and choose another more realistic description. For the structures such as those we are interested in (clusters down to small groups), almost all the mass is “made” of dark matter. In order to study the gravitational lensing of a structure properly, one has to model the gravitational potential well using the best possible knowledge for the dark matter distribution. The corrections, due to the more accurate profile distribution that we introduce, will not alter the maximum amplitude of an individual moving lens effect since it is associated with the central part of the lens. However, when dealing with some average signal coming from these secondary anisotropies, the contribution from the outskirts of the structures appears important and thus a detailed model of the matter profile is needed.

In view of the numerous recent studies on the formation of dark matter halos, which are the formation sites for the individual structures such as clusters of galaxies, we now have a rather precise idea of their formation and den-

sity profiles. Specifically, the results of Navarro, Frenk & White (1996, 1997) are particularly important. In fact, these authors have used N-body simulations to investigate the structure of dark matter halos in hierarchical cosmologies; their results put stringent constraints on the dark matter profiles. Over about four orders of magnitudes in mass (ranging from the masses of dwarf galaxy halos to those of rich clusters of galaxies), they found that the density profiles can be fitted over two decades in radius by a “universal” law (hereafter NFW profile) which seems to be the best description of the structure of dark matter halos (Huss, Jain & Steinmetz 1997). The NFW profile is given by:

$$\rho(r) = \frac{\rho_{crit} \delta_c}{(r/r_s)(1+r/r_s)^2}, \quad (2)$$

where $r_s = r_{200}/c$ is the scale radius of the halo, δ_c its characteristic overdensity, ρ_{crit} is the critical density of the universe and c is a dimensionless parameter called the concentration. The radius r_{200} is the radius of the sphere where the mean density is $200 \times \rho_{crit}$. This is what we refer to as a virialised object of mass $M_{200} = 200\rho_{crit} (4\pi/3)r_{200}^3$.

In addition to the fact that the shape is independent of the halo mass over a wide range, the NFW profile is also independent of the cosmological model. The cosmological model intervenes essentially in the formation epoch of the dark matter halo and therefore in the parameters of the profile, namely c , r_s and δ_c .

Using the density profile, one can compute the deflection angle at the impact parameter which gives the shape of the pattern and the amplitude of the induced secondary anisotropy. In our work, we compute the deflection angle following the formalism of Blandford & Kochanek (1987), which is given by the expression:

$$\delta = 2 \frac{D_{ls}}{D_{os}} \nabla_{\mathbf{r}} \int \Phi(\mathbf{r}, l) dl, \quad (3)$$

here, the integral is performed over the length element dl along the line of sight. D_{ls} and D_{os} are respectively the distances between lens and source and the observer and source. In the redshift range of the considered structures ($z < 1.5$), the distance ratios D_{ls}/D_{os} range between 1 and 0.68 for the standard CDM model, between 1 and 0.53 for the open CDM and between 1 and 0.74 for the lambda CDM model. These cosmological models will be defined in the next section. In Eq. 3 \mathbf{r} is the position of the structure and $\Phi(\mathbf{r}, l)$ is the associated gravitational potential. In order to get an analytic expression of the deflection angle and hence of the anisotropy, we used a density profile which gives a good approximation to the NFW density profile (Eq. 2), in the central part of the structure. This density profile is given by:

$$\rho(r) = \rho_{crit} \delta_c \left(\frac{r}{r_s}\right)^{-1} \exp\left(\frac{-r}{r_s}\right). \quad (4)$$

The fitted profile leads to a diverging mass at large radii and we therefore introduce a cut-off radius R_{max} to the integral. This cut-off should correspond to some physical size of the structure. With regard to the different values of the concentration c , we set $R_{max} = 8r_s$ which is in most cases equivalent to $R_{max} \simeq r_{200}$, *i.e.*, close to the virial radius. The integral giving the deflection angle is performed on the interval $[-R_{max}, R_{max}]$. For $R_{max} = 8r_s$, our fit gives a mass which is about 20% lower than the mass derived from NFW profile. This difference is larger for larger R_{max} , and for $R_{max} = 10r_s$ we find that the mass is about 33% lower. However, the larger radii the temperature fluctuations are at the 10^{-8} level. On the other hand, the Hernquist (1990) profile is also in agreement with the results of N-body simulations. Indeed, both NFW and Hernquist profiles have a similar dependence in the central part of the structure but differ at large radii where the NFW profile is proportional to r^{-3} and the Hernquist profile varies as r^{-4} . However, the amplitude of the anisotropy at large radii is very small and the results that we obtain does are not sensitive to the cut-off.

Given the peculiar velocity of the structure and its density profile, we can calculate the deflection angle (Eq. 3). Then one can determine the relative variation in frequency, $\delta\nu/\nu$, using equation 1 and thus evaluate the secondary distortion induced by a specific structure moving across the sky. We find that individual massive structures (rich galaxy clusters) produce anisotropies ranging between a few 10^{-6} to 10^{-5} ; but within a wider range of masses the amplitudes are smaller and these values are only upper limits for the moving lens effect.

3. Generalisation to a sample of structures

Future CMB (space and balloon born) experiments will measure the temperature fluctuations with very high accuracy (10^{-6}) at small angular scales. In our attempts to foresee what the CMB maps would look like and what would be the spurious contributions due to the various astrophysical foregrounds, we investigate the generalisation of the computations made above to a sample of structures. This is done in order to address the questions of the cumulative effect and contamination to the CMB.

Some work has already been done by Tuluie & Laguna 1995 and Tuluie, Laguna & Anninos 1996 who pointed out the moving lens effect in their study of the varying potential effects on the CMB. In their study, they used N-body simulations to evolve the matter inhomogeneities, from the decoupling time until the present, in which they propagated CMB photons. They have estimated the anisotropies generated by three sources of time-variations of the potential: intrinsic changes in the gravitational potential, decaying potential effect from the evolution of gravitational potential in $\Omega_0 \neq 1$ models, and peculiar bulk motions of the structures across the sky. They evaluated the contribution of the latter effect for rather

large angular scales ($\simeq 1^\circ$) due to the lack of numerical resolution (about $2h^{-1}$ Mpc) and gave estimates of the power spectrum of these effects.

With another approach, we make a similar analysis in the case of the moving lens effect extended to angular scales down to a few tens of arcseconds. We also simulate attempts at the detection and subtraction of the moving lens effect. Our approach is quite different from that of Tuluie, Laguna & Anninos, in that it is semi-empirical and apply the formalism developed for an individual structure (Sect. 2.) to each object from a sample of structures. The predicted number of objects in the sample being derived from the Press–Schechter formalism for the structure formation (Press & Schechter 1974).

3.1. Predicted population of collapsed objects

An estimate of the cumulative effect of the moving lenses requires a knowledge of the number of objects of a given mass that will contribute to the total effect at a given epoch. We assume that this number is accurately predicted by the abundance of collapsed dark matter halos as a function of their masses and redshifts, as derived using the Press–Schechter formalism. This approach was used in a previous paper (Aghanim et al. 1997) which predicted the SZ contribution to the CMB signal in a standard CDM model. In addition to the “traditional” standard Cold Dark Matter (CDM) model ($\Omega_0 = 1$), in this paper we also address the question of a generalised moving lens effect in other cosmological models. We extend the Press–Schechter formalism to an open CDM model (OCDM) with no cosmological constant ($\Omega_0 = 0.3$), and also a flat universe with a non zero cosmological constant (Λ CDM model) ($\Omega_0 = 0.3$ and $\Lambda = 0.7$). Here Ω_0 is the density parameter, Λ is the cosmological constant given in units of $3H_0^2$ and H_0 is the Hubble constant. We take $H_0 = 100h$ km/s/Mpc, and assume $h = 0.5$ throughout the paper.

In any case, the general analytic expression for the number density of spherical collapsed halos in the mass range $[M, M + dM]$ can be written as (Lacey & Cole 1993):

$$\frac{dn(M, z)}{dM} = -\sqrt{\frac{2}{\pi}} \frac{\bar{\rho}(z)}{M^2} \frac{d \ln \sigma(M)}{d \ln M} \frac{\delta_{c0}(z)}{\sigma(M)} \times \exp \left[-\frac{\delta_{c0}^2(z)}{2\sigma^2(M)} \right], \quad (5)$$

where $\bar{\rho}(z)$ is the mean background density at redshift z and $\delta_{c0}(z)$ is the overdensity of a linearly evolving structure. The mass variance $\sigma^2(M)$ of the fluctuation spectrum, filtered on mass scale M , is related to the linear power spectrum of the initial density fluctuations $P(k)$ through:

$$\sigma^2(M) = \frac{1}{2\pi^2} \int_0^\infty k^2 P(k) W^2(kR) dk,$$

where W is the Fourier transform of the window function over which the variance is smoothed (Peebles 1980) and R is the scale associated with mass M . In the assumption of a scale-free initial power spectrum with spectral index n , the variance on mass scale M can be expressed in terms of σ_8 , the *rms* density fluctuation in sphere of $8h^{-1}$ Mpc size. The relationship between these two quantities is given by (Mathiesen & Evrard 1997):

$$\sigma(M) = (1.19\Omega_0)^\alpha \sigma_8 M^{-\alpha},$$

with $\alpha = (n+3)/6$. It has been shown that σ_8 varies with the cosmological model and in particular with the density parameter Ω_0 . A general empirical fitting function ($\sigma_8 = A\Omega_0^{-B}$) was derived from a power spectrum normalisation to the cluster abundance with a rather good agreement in the values of the parameters A and B (White, Efstathiou & Frenk 1993, Eke, Cole & Frenk 1996, Viana & Liddle 1996). In our work, we use the “best fitting values” from Viana & Liddle (1996) which are $A = 0.6$ and $B = 0.36 + 0.31\Omega_0 - 0.28\Omega_0^2$ for an open CDM universe ($\Omega_0 < 1$ and $\Lambda = 0$) or $B = 0.59 - 0.16\Omega_0 + 0.06\Omega_0^2$ for a flat universe with a non zero cosmological constant ($\Omega_0 + \Lambda = 1$). We use $n = -1$ for the spectral index in the cluster mass regime which is the theoretically predicted value. Some local constraints on the temperature abundance of clusters favour $n = -2$ (Henry & Arnaud 1991, Oukbir, Bartlett & Blanchard 1997) but we did not investigate this case.

3.2. Peculiar velocities

On the scale of clusters of galaxies, typically $8h^{-1}$ Mpc, one can assume that the density fluctuations are in the linear regime. Therefore the fluctuations are closely related to the initial conditions from which the structures arise. In fact, in the assumption of an isotropic Gaussian distribution of the initial density perturbations, the initial power spectrum $P(k)$ gives a complete description of the velocity field through the three-dimensional *rms* velocity (v_{rms}) predicted by the linear gravitational instability for an irrotational field at a given scale R (Peebles 1993). This velocity is given by:

$$v_{rms} = a(t) H f(\Omega, \Lambda) \left[\frac{1}{2\pi^2} \int_0^\infty P(k) W^2(kR) dk \right]^{1/2} \quad (6)$$

where $a(t)$ is the expansion parameter, the Hubble constant H and the density parameter Ω vary with time (Caroll, Press & Turner 1992). The function $f(\Omega, \Lambda)$ is accurately approximated by $f(\Omega, \Lambda) = \Omega^{0.6}$ (Peebles 1980) even if there is a non zero cosmological constant (Lahav et al. 1991). Furthermore, under the assumptions of linear regime and Gaussian distribution of the density fluctuations, the structures move with respect to the global Hubble flow with peculiar velocities following a Gaussian distribution $f(v) = \frac{1}{v_{rms}\sqrt{2\pi}} \exp(-\frac{v^2}{2v_{rms}^2})$ which is fully described by v_{rms} . This prediction is in agreement with

numerical simulations (Bahcall et al. 1994, Moscardini et al. 1996).

The present observational status of peculiar cluster velocities puts few constraints on the cosmological models. Results from the Hudson (1994) sample using D_n - σ and IRTF distance estimators give respectively $v_{rms} = 688 \pm 82$ and 646 ± 120 km/s, a composite sample gives $v_{rms} = 725 \pm 60$ km/s (Moscardini et al 1996). Giovanelli’s (1996) sample gives a smaller value, $v_{rms} = 356 \pm 37$ km/s. In our paper we compute the three-dimensional *rms* peculiar velocity on scale $8h^{-1}$ Mpc (typical virial radius of a galaxy cluster) using Eq. 6 for the three cosmological models. This is because large scale velocities are mostly sensitive to long wavelength density fluctuations. This smoothing allows us to get rid of the nonlinear effects on small scales but it also tends to underestimate the peculiar velocities of the smallest objects that we are interested in. Nevertheless, with regard to the rather important dispersion in the observational values ($320 < v_{rms} < 780$ km/s), we use the predicted theoretical values, which range between 400 and 500 km/s, and are hence in general agreement with the observational data.

3.3. Simulations

For each cosmological model, we generate a simulated map of the moving lens effect in order to analyse the contribution to the signal in terms of temperature fluctuations. The simulations are essentially based on the studies of Aghanim et al. (1997). In the following, we describe briefly the main hypothesis that we make in simulating the maps of the temperature fluctuations induced by the moving lens effect associated with small groups and clusters of galaxies (10^{13} and $10^{15} M_\odot$). The predicted number of massive objects is derived from a distribution of sources using the Press-Schechter formalism normalised (Viana & Liddle 1996) using the X-ray temperature distribution function derived from Henry & Arnaud (1991) data. This normalisation has also been used by Mathiesen & Evrard (1997) for the ROSAT Brightest Clusters Sample compiled by Ebeling et al. (1997). The position and direction of motion of each object are random. Their peculiar velocities are also random within an assumed Gaussian distribution. Here again, the correlations were neglected because the effect is maximum very close to the central part of the structure (about 100 kpc) whereas the correlation length is between 5 and 20 Mpc (Bahcall 1988). The final maps account for the cumulative effect of the moving lenses with redshifts lower than $z = 1.5$. We refer the reader to Aghanim et al. (1997) for a detailed description of the simulation.

In this paper, some changes and improvements have been made to our previous study (Aghanim et al. 1997). In this paper, the predicted source counts (Eq. 5, Sect. 3.1) are in agreement with more recent data. They are also adapted to the various cosmological models that we

have assumed. The standard deviation of the peculiar velocity distribution is computed using equation 6 and is in reasonable agreement with the data. The advantage of using this equation is that the variations with time and cosmology are directly handled in the expression. As we pointed out in section 2, the secondary effects we study here are associated with the whole mass of the structure, not only the gas mass. Therefore, the gas part of structures are modelled using the β -profile (as in the previous case) to simulate the SZ effect. Whereas the density profile (Eq. 4) is used to simulate the potential well of the moving lens effect. We note that the results of the N-body simulations of Navarro, Frenk & White (1996) are consistent with the assumption of an intra-cluster isothermal gas in hydrostatic equilibrium with a NFW halo.

4. Results of the data analysis

We analyse the simulated maps of secondary fluctuations due to the moving lens effect, for the three cosmological models described in Sect. 3, and we quantify their contributions. We also make attempts at detecting and extracting the secondary fluctuations from the entire signal (primary CMB, SZ kinetic effect and moving lenses).

4.1. Statistical analysis

We show the histogram of the secondary fluctuations for the moving lens effect (randomly generated) in the three cosmogonies (Fig. 2). In all cases, the amplitude of anisotropies ranges roughly between $\delta T/T \simeq -1.5 \cdot 10^{-5}$ and $\delta T/T \simeq 1.5 \cdot 10^{-5}$. The *rms* value of the anisotropies varies a little with the cosmological model $(\frac{\delta T}{T})_{rms}^{CDM} \simeq 5.2 \cdot 10^{-7}$, $(\frac{\delta T}{T})_{rms}^{\Lambda CDM} \simeq 3.4 \cdot 10^{-7}$ and finally $(\frac{\delta T}{T})_{rms}^{OCDM} \simeq 3.5 \cdot 10^{-7}$. Our results are in general agreement with those of Tuluie, Laguna & Anninos (1996). In all the cosmological models, the *rms* value of the anisotropies is about a factor 10 lower than the *rms* amplitude of the fluctuations due to the SZ kinetic effect associated with the same structures, which is about $5 \cdot 10^{-6}$; and is about 30 times lower than the $(\frac{\delta T}{T})_{rms}$ of the primary fluctuations in a standard CDM model. The distribution of the temperature fluctuations induced by moving lenses exhibits a highly non Gaussian signature (Fig. 2). The fourth moment of the distribution, called the kurtosis, measures the peakedness or flatness of the distribution relative to the normal one. We find that the kurtosis for the standard CDM, OCDM and Λ CDM models are positive and respectively equal to about 51, 97 and 41. The distributions are thus peaked (leptokurtics).

In the context of our statistical analysis of the secondary anisotropies, we also compute the fitted angular power spectra (Fig. 3) of the three main sources of anisotropies: primary CMB fluctuations (in the standard CDM model) and both the predicted power spectra of the fluctuations due to the moving lenses (thin lines) and the

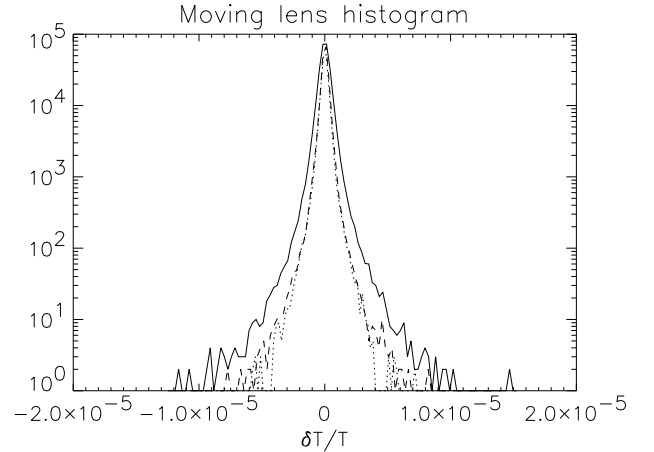


Fig. 2. Histograms showing the distributions of the secondary fluctuations in the simulated maps. The solid, dashed and dotted lines are for respectively the standard, Open and Lambda CDM model.

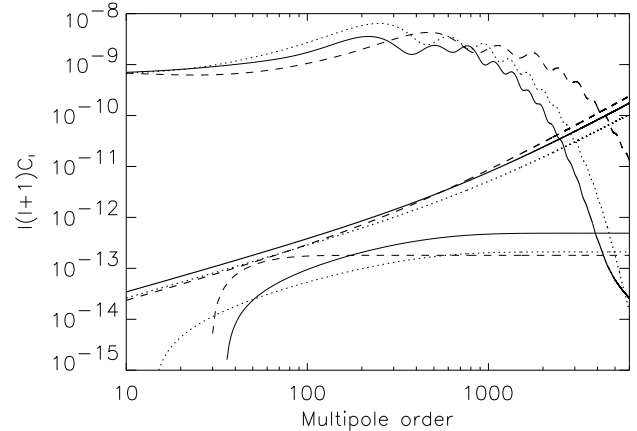


Fig. 3. Power spectra of the primary fluctuations obtained using the CMBFAST code compared to the fitted power spectra of the secondary fluctuations due to the Sunyaev-Zel'dovich kinetic effect (thick lines) and to the moving lens effect (thin lines). The power spectra for the standard CDM model (solid line), open CDM model (dashed line) and lambda CDM model (dotted line) are shown.

SZ kinetic effect (thick lines). In figure 3, the solid lines are for the standard CDM model, dashed and dotted lines are respectively for the open and non zero cosmological constant models. We fit the power spectra of the secondary anisotropies due to moving lenses with the general expression:

$$l(l+1)C_l = a_{ls} - b_{ls} \exp(-c_{ls}l), \quad (7)$$

in which the fitting parameters for every cosmological model are given in table 1. The SZ kinetic anisotropies

Table 1. *Fitting parameters for the power spectrum of the fluctuations induced by moving lenses as a function of the cosmological model.*

	a_{ls}	b_{ls}	c_{ls}
SCDM	$4.9 \cdot 10^{-13}$	$5.5 \cdot 10^{-13}$	$3.3 \cdot 10^{-3}$
OCDM	$1.8 \cdot 10^{-13}$	$7.6 \cdot 10^{-13}$	$4.9 \cdot 10^{-2}$
Λ CDM	$2.1 \cdot 10^{-13}$	$2.2 \cdot 10^{-13}$	$3.4 \cdot 10^{-3}$

Table 2. *Fitting parameters for the power spectrum of the fluctuations induced by the Sunyaev–Zel’dovich kinetic effect as a function of the cosmological model.*

	a_{SZ}	b_{SZ}
SCDM	$3.4 \cdot 10^{-15}$	$4.3 \cdot 10^{-18}$
OCDM	$2.3 \cdot 10^{-15}$	$6.3 \cdot 10^{-18}$
Λ CDM	$2.6 \cdot 10^{-15}$	$2.5 \cdot 10^{-18}$

are fitted with the following expression:

$$l(l+1)C_l = a_{SZ}l + b_{SZ}l^2, \quad (8)$$

with the fitting parameters for the cosmological models gathered in table. 2.

The power spectra of the SZ kinetic effect exhibit the characteristic l^2 dependence on small angular scales for the point-like source dominated signal. All the power spectra have rather similar amplitudes, at large scales, in particular up to $l \simeq 200$ where we notice an excess of power at small angular scales in the OCDM model. This is because low Ω_0 models produce higher counts than $\Omega_0 = 1$ models (Barbosa et al. 1996).

The moving lens power spectra, for both CDM and Λ CDM models, exhibit a plateau at $l > 500$ with a decrease at larger angular scales. For the OCDM model, the dependence is roughly constant at all scales. We also note that the highest and lowest power are obtained, at small angular scales, for respectively the standard CDM and OCDM models. At large scales, the opposite is true.

In order to interpret this behaviour, we distinguish between what we refer to as the resolved and unresolved structures. The spatial extent of the resolved structures is much greater than the pixel size (or analogously the beam size). Whereas, the unresolved objects have extents close to, or smaller than, the pixel size. At the pixel size an unresolved structure generates a SZ kinetic anisotropy which is averaged to a non-zero value. Whereas the dipolar anisotropy induced by the moving lens effect is averaged to zero (except what remains from the side effects). A pixel size anisotropy thus does not contribute to the signal in the moving lens effect; while it contributes with its $\delta T/T$ amplitude in the SZ kinetic effect. As a result, the distribution of the moving lens anisotropies does not reflect the whole population of objects, but only the distribution of the resolved ones. In the OCDM model the

structures are more numerous and form earlier than in a standard CDM model. Consequently, the distribution of unresolved objects in OCDM thus shows a large excess compared with the standard CDM and there are less resolved structures in the OCDM model than in the CDM. The excess of power in the the moving lens fluctuations spectrum (Fig. 3, solid line) reflects the dependence of the size distribution upon the cosmological model.

At a given large scale and for the SZ kinetic effect, there is more power on large scales in a standard CDM model compared with the OCDM. This is because the contribution to the power comes from low redshift resolved structures, which are less numerous in an OCDM model. Consequently, in the case of the fluctuations induced by the moving lens effect at large scale, the power in the OCDM model is greater than in the standard CDM. In addition, at a given large scale the power of the moving lens effect accounts for the cumulative contribution from the massive objects, with high amplitude, and from the less massive ones, with lower amplitudes.

A comparison between the CMB and the moving lens power spectra obviously shows that primary CMB fluctuations dominate at all scales larger than the cut-off scale, whatever the cosmological model (Fig. 3). Furthermore in the OCDM and Λ CDM models the cut-off is shifted towards smaller angular scales making the CMB the dominant contribution over a larger range of scales. The most favourable configuration to study and analyse the fluctuations is therefore the CDM model since it gives the largest cut-off scale compared to the other cosmological models and since it gives the highest prediction for the power of the moving lens effect. The level of spurious additional signal associated with the moving lens effect is negligible compared to both the primary and SZ kinetic fluctuations. Below the scale of the cut-off in the CMB power spectrum, the l^2 dependence of the SZ fluctuations is dominant over the moving lens effect. Moreover, contrary to the thermal effect, the SZ kinetic, moving lens and primary fluctuations have black body spectra. This makes the spectral confusion between them a crucial problem. At small angular scales, the SZ kinetic effect represents the principal source of confusion.

Nevertheless, the contribution of the SZ kinetic effect is very dependent on the predicted number of structures that show a gas component. In other words, some objects like small groups of galaxies may not have a gas component, and therefore no SZ thermal or kinetic anisotropy is generated, but they still exhibit the anisotropy associated with their motion across the sky. We attempt to study a rather wide range of models. We therefore use two prescriptions to discriminate between “gaseous” objects and “non gaseous” ones. These prescriptions correspond to arbitrary limits on the masses of the structures. Namely: in the first model, we assume that all the dark matter halos with masses greater than $10^{13} M_{\odot}$ have a gas fraction of 20% and exhibit SZ thermal and kinetic anisotropies;

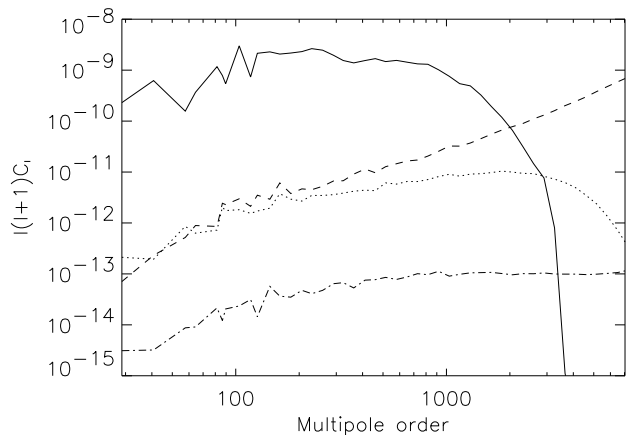


Fig. 4. Randomly generated power spectra of the primary fluctuations in the standard CDM model (solid line) compared to the secondary fluctuations due to the moving lens effect (dashed-dotted line) and the Sunyaev-Zel’dovich kinetic effect with a cut-off at $10^{13} M_{\odot}$ (dashed line) and at $10^{14} M_{\odot}$ (dotted line).

while in the second model, it is only the structures with masses $M \geq 10^{14} M_{\odot}$ which produce SZ anisotropies. We ran the simulations with both assumptions in the standard CDM model and computed the corresponding power spectra (Fig. 4). The power spectrum associated with the SZ kinetic effect shows, as expected, that the cut-off in masses induces a decrease in the power of the SZ kinetic effect on all scales, and in particular on very small scales with a cut-off at $l \simeq 4000$. The power spectrum of the SZ kinetic anisotropies can be fitted with the following expression:

$$l(l+1)C_l = -3.3 \cdot 10^{-13} + 1.6 \cdot 10^{-14} l \exp(6.2 \cdot 10^{-4} l). \quad (9)$$

Despite this cut-off in mass and the decrease in power, the SZ kinetic effect remains much larger than the moving lens effect. Therefore at small angular scales, the SZ kinetic point like sources are still the major source of confusion. In order to get rid of this pollution in an effective way, one would need a very sharp but unrealistic cut-off in mass.

4.2. Detection and extraction

We analyse the simulated maps in order to estimate the amplitudes of the anisotropies associated with each individual moving structure. In such an analysis both primary CMB and SZ kinetic fluctuations represent spurious signals with regards to the moving lens. Figure 3 shows that these signals contribute at different scales and at different levels. The primary CMB contribution vanishes on scales lower than the cut-off whereas the SZ kinetic contribution shows up at all scales and its power increases as l^2 on small scales. This indicates clearly that the most important problem with the analysis of the maps (extrac-

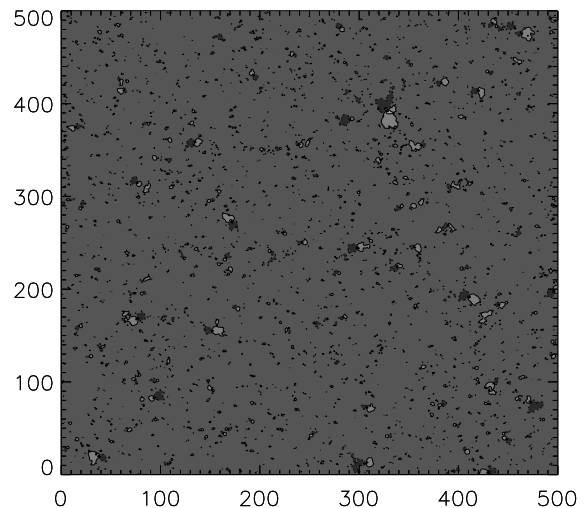


Fig. 5. Plot showing the contours superimposed over a simulated map of the fluctuations induced by moving lenses in the standard CDM model (pixel size = $1.5'$). The contour levels and grey scales shown in the plot are: $1.5 \cdot 10^{-5}$, $\pm 1 \cdot 10^{-5}$, $\pm 5 \cdot 10^{-6}$, $\pm 1 \cdot 10^{-6}$

tion and detection of the moving lens anisotropy) is the confusion due to the point-like sources. This problem is made worse by spectral confusion. A compromise must be found between investigating scales smaller than the CMB cut-off, which maximises the pollution due to SZ kinetic effect, and exploring larger scales where the SZ contribution is low (but still 10 times larger than the moving lenses). The main problem here is that on these scales the primary fluctuations are 100 times larger than the moving lenses which makes their detection hopeless.

Nevertheless, the signal has two characteristics that make the attempts at detection worthy at small scales. The first advantage is that the anisotropy induced by a moving lens exhibits a particular spatial signature which is seen as the dipole-like patterns shown in figure 5. The second, and main advantage is that we know the position of the center of the structures thanks to the SZ thermal effect.

In fact, the objects giving rise to a dipole-like anisotropy are either small groups or clusters of galaxies with hot ionised gas which also exhibit SZ thermal distortions. The latter, characterised by the so-called Comptonisation parameter y , have a very specific spectral signature. It is therefore rather easy to determine the position of the center of a structure assuming that it corresponds to the maximum value of the y parameter. In the context of the Planck multi-wavelength experiment for CMB observations, it was shown (Aghanim et al. 1997) that the location of massive clusters will be well known because of the presence of the SZ thermal effect.

We based our detection strategy for the moving lens effect on these two properties (spatial signature and known location). We also assumed that the SZ thermal effect was perfectly separated from the other contributions thanks to the spectral signature. The problem is therefore eased since it lies in the separation of moving lens, SZ kinetic and primary CMB anisotropies *at known positions*. Nevertheless the clusters and their gravitational potential wells are likely to be non-spherical, making the separation difficult. In the following, we will show that even in the simple spherical model we adopt the separation remains very difficult because of the spectral confusion of the moving lens, SZ kinetic and primary CMB fluctuations. Separation is even more difficult because of the numerous point-like SZ kinetic sources corresponding to weak clusters and small groups of galaxies for which we do not observe the SZ thermal effect.

4.2.1. Method

In order to clean the maps from the noise (SZ kinetic and CMB fluctuations), we filter them using a wavelet transform. Wavelet transforms have received significant attention recently due to their suitability for a number of important signal and image processing tasks. The principle behind the wavelet transform, as described by Grossmann & Morlet (1984), Daubechies (1988) and Mallat (1989) is to hierarchically decompose an input image into a series of successively lower resolution reference images and associated detail images. At each level, the reference image and detail image contain the information needed to reconstruct the reference image at the next higher resolution level. So, what makes the wavelet transform interesting in image processing is that, unlike Fourier transform, wavelets are quite localised in space. Simultaneously, like the Fourier transform, wavelets are also quite localised in frequency, or more precisely, on characteristic scales. Therefore, the multi-scale approach provides an elegant and powerful framework for our image analysis because the features of interest in an image (dipole pattern) are generally present at different characteristic scales. Furthermore, the wavelet transform performs contemporaneously a hierarchical analysis in both the space and frequency domains.

The maps are decomposed in terms of a wavelet basis that has the best impulse response and lowest shift variance among a set of wavelets that were tested for image compression (Villasenor et al. 1995). These two characteristics are important if we want to identify the locations and the amplitudes of the moving lenses. Since the moving lenses induce very small scale anisotropies compared to the CMB, we filter the largest scales in order to separate these two contributions. We note that this also allows us to separate the contributions due to the large scale SZ kinetic sources. In the following we describe our analysis

method, first applied to an unrealistic study case and then to a realistic case.

Study case

We filter the large scales of a map of CMB+moving lens fluctuations (no SZ kinetic contribution) in order to test the robustness and efficiency of the wavelet transform filtering. In this case, the noise due to the CMB is efficiently cleaned. In fact, Figure 6 lower left panel shows a residual signal (symbolised by the dots) associated with the moving lens fluctuations, which are simulated in the upper right panel of the same figure. We have confirmed that the positions of the residual signal agree with the positions of the input structures. Moreover, we were able to successfully extract the secondary fluctuations due to the moving lenses, as well as estimate their average peak to peak $\delta T/T$ values. Figure 8 shows the average peak to peak amplitudes of the input simulated fluctuations (solid line) and the extracted values (dashed line). The main features are well-recovered, although the amplitudes suffer from the smoothing of the filtering procedure. In this study case, with no SZ kinetic contribution, we find a correlation coefficient between input and recovered values of about 0.95.

Realistic case

When this method is applied to filter a map containing all contributions (CMB + SZ kinetic + moving lenses), we are no longer able to identify or locate the moving lens fluctuations, as shown in fig.6 lower right panel. Here, the CMB which dominates at large scales is cleaned, whereas the SZ kinetic effect, which is mainly a point-like dominated signal, at least one order of magnitude larger than the power of the moving lenses, is not cleaned and remains in the filtered signal. We have filtered at several angular scales without any positive result. On large scales the extended dipole patterns are polluted by the CMB, as mentioned above, and on small scales the SZ kinetic fluctuations are of the same scale as the moving lens anisotropies. We also tried the convolution of the total map (CMB + SZ kinetic + moving lenses) with the dipole pattern function but we were still unable to recover the moving lens fluctuations. In fact, the combination of two SZ kinetic sources, one coming forward and the other going backward, mimics a dipole-like pattern. In order to distinguish between an intrinsic dipole due to a lens and a coincidence, one needs to know a priori the direction of the motion which is of course not possible. During our analysis, we investigated two cases for the cut off in mass as describe in Sect 4.1. For the simulations with cut-off mass $10^{14} M_{\odot}$ the resulting background due to point-like SZ fluctuations is lower than the cut-off at $10^{13} M_{\odot}$ case; but we were still unable to recover the moving lens fluctuations.

In our attempt at taking advantage of the spatial signature of the moving lens fluctuations, we have located the coefficients in the wavelet decomposition that are principally associated with the moving lenses and selected them

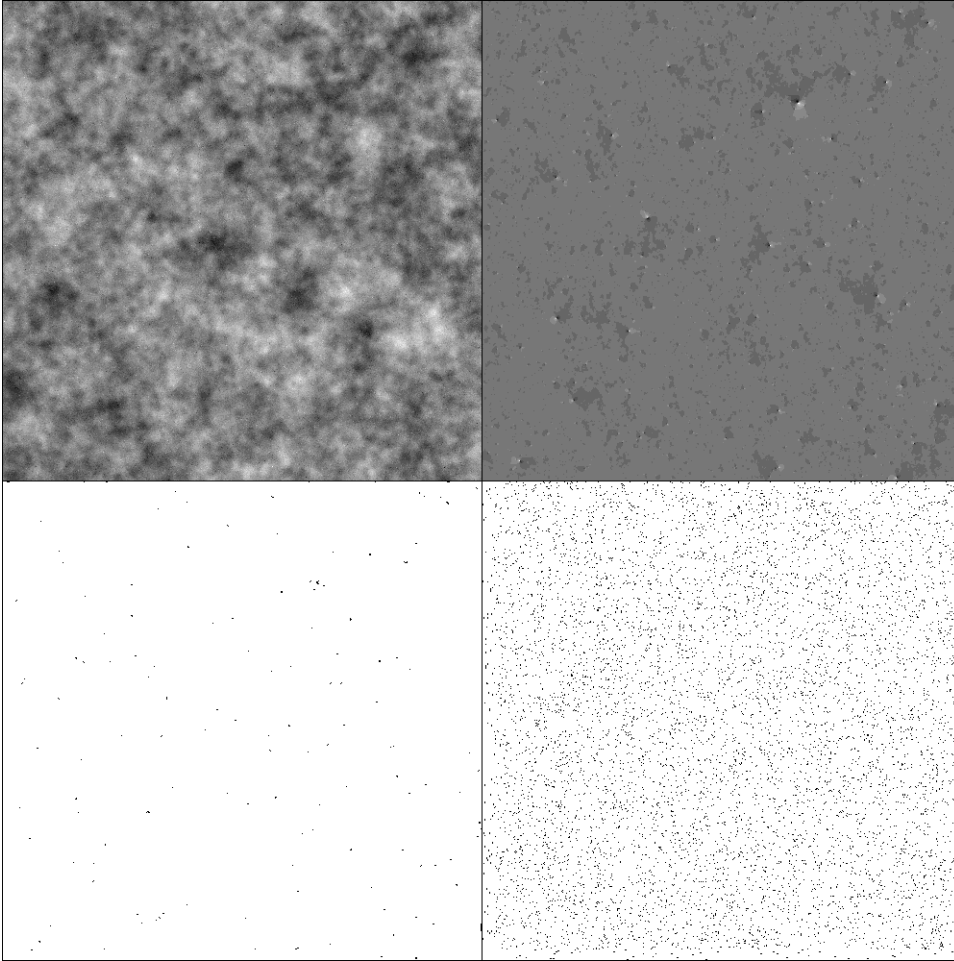


Fig. 6. The two upper panels show simulated maps: on the left, total map of the fluctuations (CMB+SZ+lens) linear scale between $1.4 \cdot 10^{-4}$ (white) and $-1.3 \cdot 10^{-4}$ (black). On the right is shown the map of the moving lenses fluctuations (linear scale between $1.5 \cdot 10^{-5}$ (white) and $-1.2 \cdot 10^{-5}$ (black)). The two lower panels are the result of the wavelet filtering process. The left panel is for a CMB+lens configuration, in which we notice that the secondary anisotropies are rather well extracted. The right panel represents the case of all contributors and shows that the moving lenses are completely dominated by the SZ kinetic noise.

from all the wavelet coefficients. Our study case procedure is the following. We make the wavelet transform for the moving lens fluctuations and, separately, we also make the transform for the remaining signals (CMB + SZ kinetic). We locate the wavelet coefficients for the moving lenses whose absolute values are higher than the absolute values of CMB+SZ kinetic coefficients. Then, we select, in the transform of the total fluctuation map (CMB + SZ + lenses), the coefficients corresponding to the previously located ones. Finally we perform the inverse transform on the map (CMB + SZ + lenses) according to the selected coefficients. When we compare the average peak to peak amplitudes of the recovered (Fig. 7: dashed line and Fig. 8: dotted-dashed line) and input (Fig. 7 and Fig. 8, solid line) lens fluctuations, we find a very good correlation between the amplitudes of the original and the reconstructed moving lens fluctuations. The correlation factor is of the order of 0.7 for CMB + SZ + lenses with a cut-off mass at

$10^{13} M_{\odot}$ and higher than 0.9 with the cut-off at $10^{14} M_{\odot}$. This difference between the correlation factors is an effect of the cut-off in masses. In fact, for the $10^{14} M_{\odot}$ cut-off, the filtered maps are cleaner than for the $10^{13} M_{\odot}$ cut-off. Therefore, in the latter case some of the lenses have very little or no signature in the wavelet decomposition, hence they are not recovered and the correlation factor decreases.

The results of our study case confirm that the moving lens fluctuations have a significant spatial signature in the total signal although their amplitudes are very low compared with the CMB and SZ fluctuations. However, it is worth noting that such a “good” result is obtained only because we use sorted coefficients from two separated maps, one containing the lens signal and the other containing the polluting signals. In a real case, there is no way to separate the contributions because of the spectral confusion and therefore there is no a priori knowledge of the “right”

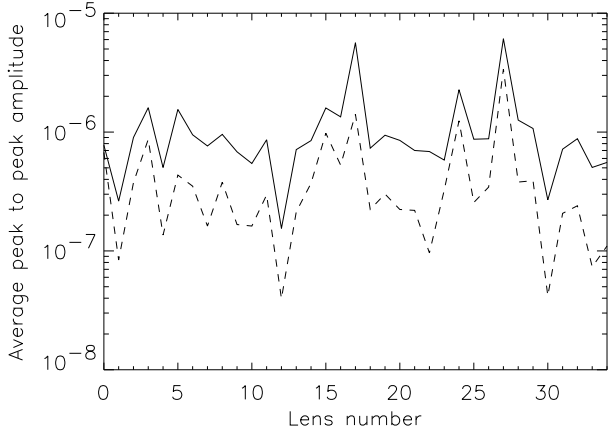


Fig. 7. Average peak to peak amplitude of the secondary anisotropies due to the moving lenses (cut-off mass $10^{14} M_{\odot}$) for lenses with a decreasing y parameter. The solid line represents the amplitudes in the original simulated lenses map. The dashed line represents the extracted amplitudes **after sorting the wavelet coefficients and filtering all contributions (CMB+SZ+lenses)**. The correlation factor is equal to 0.9.

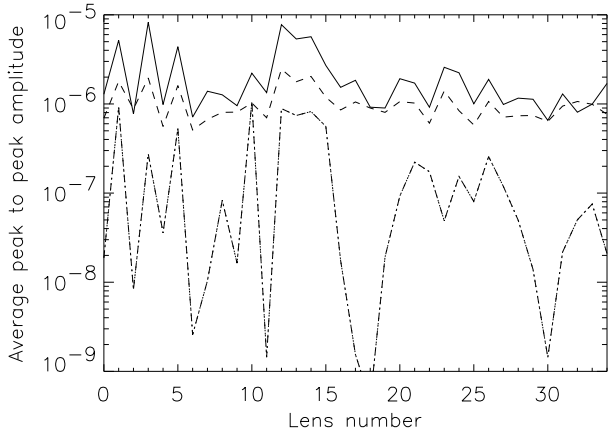


Fig. 8. Average peak to peak amplitude of the secondary anisotropies due to the moving lenses (cut-off mass $10^{13} M_{\odot}$) for lenses with decreasing y parameter. Solid line represents the amplitudes in the original simulated lens map. The dashed line represents the extracted amplitudes without sorting the wavelet coefficients and after filtering the CMB+lenses contributions (no SZ kinetic). The dotted-dashed line represents the extracted amplitudes after sorting the wavelet coefficients and filtering all contributions (CMB+lenses+SZ kinetic).

coefficients in the wavelet decomposition. In our analysis, we tried several sorting criteria for the coefficients but we could not find a robust and trustworthy criterion to reproducibly discriminate between the wavelet coefficients belonging to the moving lens fluctuations and the coefficients belonging to the noise (SZ kinetic and CMB fluctuations).

During the analysis, we could not overcome the physical limitation corresponding to the presence of sources of SZ kinetic anisotropies at the same scale and with amplitudes at least 10 times higher than the signal (moving lens fluctuations).

5. Conclusions

In our work, we investigate the secondary fluctuations induced by moving lenses with masses ranging from those of groups of galaxies to those of clusters of galaxies in a simple way, based on predicted structure counts and simulated maps. This method allows us to explore a rather wide range of scales (> 10 arcseconds) in various cosmological models. The analysis, in terms of angular power spectra, show the scales for which the primary fluctuations are dominant (Fig. 3). In the standard and lambda CDM models, the primary anisotropies are dominant respectively for scales $l < 4000$ and $l < 4500$ whereas in the Open CDM model they are dominant for $l < 6000$. In practice, it is thus impossible to detect the secondary anisotropies due to moving lenses in the open model. The standard CDM model shows the smallest cut-off scale with an intermediate SZ kinetic pollution, compared to the other two models. It is therefore the “best case” framework for making an analysis and predicting the detection of fluctuations and the contributions that they induce. One must keep in mind that the results quoted in this particular case represent the “best” results we get from the analysis.

The results of our analysis are obtained under the assumption of a universe that never re-ionises, which is of course not the case. The re-ionisation, if it is homogeneous, is supposed to somewhat ease the task of extraction of the pattern. In fact, its main effect is to damp the angular power spectrum of the primary anisotropies on small scales, shifting the cut-off towards larger scales. In this case, the effect of moving lenses dominates over the CMB fluctuations, and the SZ kinetic is not as high as it is on very small scales. However, if the re-ionisation is late and inhomogeneous, it generates additional SZ kinetic-type secondary fluctuations (Aghanim et al. 1996) without damping the power spectrum by more than a few percent. Here, the re-ionisation might worsen the analysis at small scales. In any case, there could be some other additional secondary fluctuations principally due to the Vishniac effect, that arise in a re-ionised universe. Our work thus gives a “best case” configuration of the problem, with all other effects tending to worsen the situation.

We found that the secondary fluctuations induced by the moving gravitational lenses can be as high as $1.5 \cdot 10^{-5}$; with *rms* contributions of about 5 to $3 \cdot 10^{-7}$ in the three cosmological models. Even if the moving lens fluctuations have a particular dipolar pattern and even if they are “perfectly” located through their SZ thermal effect, the detection of the moving lens effect and its separation from the

SZ kinetic and primary fluctuations are very difficult because of the very high level of confusion, on the scales of interest, with the point-like SZ kinetic anisotropies and because of spectral confusion.

We nevertheless analysed the simulated maps using an adapted wavelet technique in order to extract the moving lens fluctuations. We conclude that *the contribution of the secondary anisotropies due to the moving lenses is thus negligible whatever the cosmological model. Therefore it will not affect the future CMB measurements except as a background contribution. We have highlighted the fact that the moving lens fluctuations have a very significant spatial signature but we did not succeed in separating this contribution from the other signals.*

Acknowledgements. The authors wish to thank J.-L. Puget for many suggestions and fruitful discussions. They wish to thank the referee, M. Birkinshaw, for his helpful comments that much improved the paper. The authors thank J.F. Navarro, C. Frenk and S.D. White for kindly providing us a FORTRAN routine, computing the concentrations and the critical densities of the dark matter profiles, and J.R. Bond for providing the CMB map used in the analysis. The power spectra of the primary fluctuations were performed using the CMBFAST code (M. Zaldarriaga & U. Seljak). In addition, we thank F. Bernardeau, F.-X. Désert, Y. Mellier and J. Silk for helpful discussions and A. Jones for his careful reading of the paper.

References

- Aghanim, N., Désert, F.-X., Puget, J.-L., Gispert, R. 1996, *A&A*, **311**, 1
- Aghanim, N., De Luca, A., Bouchet, F.R., Gispert, R., Puget, J.-L. 1997, *A&A*, **325**, 9
- Bahcall, N.A. 1988, *ARA&A*, **26**, 631
- Bahcall, N.A., Cen, R., Gramann, M. 1994, *ApJ*, **430**, 13
- Barbosa, D., Bartlett, J.G., Blanchard, A., Oukbir, J. 1996, *A&A*, **314**, 13
- Birkinshaw, M. 1989, in *Moving Gravitational lenses*, p. 59, eds. J. Moran, J. Hewitt & K.Y. Lo; Springer-Verlag, Berlin
- Birkinshaw, M. 1997, *preprint*
- Birkinshaw, M., Gull, S.F. 1983, *Nature*, **302**, 315
- Blandford, R.D., Kochanek, C.S. 1987, *ApJ*, **321**, 658
- Bouchet, F.R., Bennett, D.P., Stebbins, A. 1988, *Nature*, **335**, 410
- Carroll, S.M., Press, W.H., Turner, E.L. 1992, *ARA&A*, **30**, 499
- Daubechies, I. 1988, *Commun. Pure Appl. Math.*, **vol. XLI**, 909
- Dodelson, S., & Jubas, J.M. 1995, *ApJ*, **439**, 503
- Ebeling, H., Edge, A.C., Fabian, A.C., Allen, S.W., Crawford, C.S., Böhringer, H. 1997, *ApJ Lett.*, **479**, 101
- Eke, V.R., Cole, S., Frenk, C.S. 1996, *M.N.R.A.S.*, **282**, 263
- Giovanelli, R., Haynes, M.P., Wegner, G., Da Costa, L.N., Freudling, W., Salzer, J.J. 1996, *ApJ*, **464**, 99
- Grossmann, A., Morlet, J. 1984, *SIAM J. Math. Anal.*, **15**, 723
- Henry, J.P., Arnaud, K.A. 1991, *ApJ*, **372**, 410
- Hernquist, L., 1990, *ApJ*, **356**, 359
- Hudson, M.J. 1994, *M.N.R.A.S.*, **266**, 468
- Huss, A., Jain, B., Steinmetz, M. 1997, *astro-ph/9703014*
- Kaiser, N. 1982, *M.N.R.A.S.*, **198**, 1033
- Kaiser, N., Stebbins, A. 1984, *Nature*, **310**, 391
- Kamionkowski, M., Spergel, D.N., Sugiyama, N. 1994, *ApJ Lett.*, **426**, 57
- Lacey, C., Cole, S. 1993, *M.N.R.A.S.*, **262**, 627
- Lahav, O., Rees, M.J., Lilje, P.B., Primack, J.R. 1991, *M.N.R.A.S.*, **251**, 128
- Mallat, S. 1989, *IEEE Trans. Patt. Anal. Machine Intell.*, **7**, 674
- Martinez-González, E., Sanz, J.-L., & Silk, J. 1990, *ApJ*, **355**, L5
- Mathiesen, B., Evrard, A.E. 1997, *astro-ph/9703176*
- Moscardini, L., Branchini, E., Brunozzi, P.T., Borgani, S., Plioinis, M., Coles P. 1996, *M.N.R.A.S.*, **282**, 384
- Navarro, J.F., Frenk, C.S., White, S.D.M. 1996, *ApJ*, **462**, 563
- Navarro, J.F., Frenk, C.S., White, S.D.M. 1997, *ApJ*, **490**, 493
- Oukbir, J., Bartlett, J.G., Blanchard, A. 1997, *A&A*, **320**, 365
- Peebles, P.J.E. 1980, in *The Large Scale Structure of the Universe*, Princeton University Press
- Peebles, P.J.E. 1993, in *Principles of Physical Cosmology*, Princeton University Press
- Press, W., Schechter, P. 1974, *ApJ*, **187**, 425
- Rees, M.J., Sciama, D.W. 1968, *Nature*, **511**, 611
- Rephaeli, Y. 1995, *ARA&A*, **33**, 541
- Sachs, R.K., Wolfe, A.M. 1967, *ApJ*, **147**, 73
- Seljak, U. 1996, *ApJ*, **463**, 1
- Smoot, G., et al., 1992, *ApJ*, **396**, 1
- Sunyaev, R.A., Zeldovich, Ya.B. 1972, *A&A*, **20**, 189
- Sunyaev R.A., Zeldovich, Ya.B. 1980, *M.N.R.A.S.*, **190**, 413
- Tuluie, R., Laguna, P. 1995, *ApJ Lett.*, **445**, L73
- Tuluie, R., Laguna, P., Anninos, P. 1996, *ApJ*, **463**, 15
- Viana, P.T.P., Liddle, A.R. 1996, *M.N.R.A.S.*, **281**, 323
- Villasenor, J.D., Belzer, B., Liao, J. 1995, *IEEE Trans. Im. Proc.*, **8**, 1057
- Vishniac, E. T. 1987, *ApJ*, **322**, 597
- White, S.D.M., Efstathiou, G., Frenk, C.S. 1993, *M.N.R. A.S.*, **262**, 1023